LAWRENCE
LIVERMORE
NATIONAL
LABORATORY

LLNL-JRNL-411429

# Model Studies of the Dynamics of Bacterial Flagellar Motors

F. Bai, C. Lo, R. Berry, J. Xing

March 20, 2009

Biophysical Journal

**Disclaimer**

This document was prepared as an account of work sponsored by an agency of the United States government. Neither the United States government nor Lawrence Livermore National Security, LLC, nor any of their employees makes any warranty, expressed or implied, or assumes any legal liability or responsibility for the accuracy, completeness, or usefulness of any information, apparatus, product, or process disclosed, or represents that its use would not infringe privately owned rights. Reference herein to any specific commercial product, process, or service by trade name, trademark, manufacturer, or otherwise does not necessarily constitute or imply its endorsement, recommendation, or favoring by the United States government or Lawrence Livermore National Security, LLC. The views and opinions of authors expressed herein do not necessarily state or reflect those of the United States government or Lawrence Livermore National Security, LLC, and shall not be used for advertising or product endorsement purposes.

# Model Studies of the Dynamics of Bacterial Flagellar Motors

**Fan Bai[1], Chien-Jung Lo[1], Richard M. Berry[1], and Jianhua Xing[2, 3, 4],**

[1.] Clarendon Laboratory, Department of Physics, University of Oxford, Oxford, OX1 3PU, UK

[2.] Chemistry, Materials, and Life Sciences Directorate, University of California & Lawrence Livermore National Laboratory, Livermore, CA 94550

[3.] Department of Biological Sciences, Virginia Polytechnic Institute and State University, Blacksburg, VA, 24061-0406

[4.] Send correspondences to: jxing@vt.edu

# ABSTRACT

The Bacterial Flagellar Motor is a rotary molecular machine that rotates the helical filaments which propel swimming bacteria. Extensive experimental and theoretical studies exist on the structure, assembly, energy input, power generation and switching mechanism of the motor. In our previous paper (*Proc. Natl. Acad. Sci, 103:1260 (2006)*), we explained the general physics underneath the observed torque-speed curves with a simple two-state Fokker-Planck model. Here we further analyze this model. In this paper we show 1) the model predicts that the two components of the ion motive force can affect the motor dynamics differently, in agreement with the latest experiment by Lo *et al.(Biophys. J., 93:294 (2007)*; 2) with explicit consideration of the stator spring, the model also explains the lack of dependence of the zero-load speed on stator number in the proton motor, recently observed by Yuan and Berg (*Proc. Natl. Acad. Sci, 105:1182 (2008)*); 3) the model reproduces the stepping behavior of the motor even with the existence of the stator springs and predicts the dwelling time distribution. Predicted stepping behavior of motors with two stators is discussed, and we suggest future experimental verification.

# INTRODUCTION

Flagellar rotation is one of the major mechanisms for bacterial motility. Using the transmembrane electrochemical $H^+$ (or $Na^+$) gradient to power rotation of the flagellar motor, free-swimming bacteria can propel their cell body at a speed of 15-100 μm/s, or up to 100 cell body lengths per second (1, 2). The proton motive force (PMF) is a sum of enthalpic and entropic terms:

$$\Delta\tilde{\mu} \equiv pmf = \underbrace{\Delta\psi}_{\substack{\text{membrane}\\\text{potential}}} + \underbrace{2.303\,\frac{k_{\mathrm{B}}T}{e}\,\Delta pH}_{\substack{\text{Transmembrane ion}\\\text{concentration gradient}}}. \tag{1}$$

In the case of a sodium driven motor, $\Delta pH$ is replaced by the sodium ion concentration term $\Delta pNa = -\log_{10}([Na^+]_{in}/[Na^+]_{out})$. The Bacterial Flagellar Motor (BFM) consists of a rotary motor embedded in the cell envelope connected to an extracellular helical propeller (see Fig.1a) (1, 3, 4). The motor is the first natural object proposed and demonstrated to be a rotary machine (5). It is about 45 nm in diameter and contains about eleven torque-generating units attached to the cell wall around the periphery of the rotor (6). The stator is believed to deliver torque to the rotor by converting the free energy of inward flow of ions down an electrochemical gradient across the cytoplasmic membrane into the cell.

A schematic plot of the key components of the *Escherichia coli* bacterial flagellar motor is given in Fig.1a, derived from collected research of electron microscopy, sequencing and mutational studies (reviewed in refs (7, 8)). More recently, crystal structures of some of the rotor proteins have become available (7). The basal body comprises a rod connecting four protein rings, the L-ring, P-ring, MS-ring, and cytoplasmic C-ring (9). Functionally, the basal body is the rotor of the BFM. The rotor complex is homologous to the type-III secretion system of Gram negative bacteria (9, 10). Around the periphery of the MS-ring, there is a circular array of stator complexes. They comprise the MotA and MotB proteins in a 4A2B stoichiometry. The MotA/MotB complex is homologous to the TonB-ExbB-ExbD and the TolA-TolQ-TolR complexes of outer membrane transport energizers (11, 12). Both MotA and MotB span the cytoplasmic membrane. MotB is suggested to anchor MotA to the rigid framework of the peptidoglycan through some 7-8 nanometer long α-helices (the so-called stator springs in the later discussions). MotA has four transmembrane $\alpha$ -helices and a large cytoplasmic loop. Mutational studies found that several critical charged residues on these cytoplasmic loop interact electrostatically with charged residues on the C-terminus of FliG on the C-ring (13). This interaction is important for the torque generation mechanism of the BFM. FliG, FliM, and FliN constitute the C ring and are also referred to as the "switch complex", since mutations in this region often lead to defects in switching function. The structure of the $Na^+$ motor is similar to the $H^+$ motor. The MotA/MotB complex correspondence is the PomA/PomB complex in the $Na^+$ motor (14). The $Na^+$ and $H^+$ motors probably have the same mechanism. This idea is supported by the experimental observation that chimeric motors that mix components from both types of motor can still function (15). In the rest of this paper we will refer to one particular $Na^+$-driven chimeric motor which uses a $Na^+$ type stator and *E. coli* BFM rotor (15). Since it is easier to change the $Na^+$ concentration and sodium-motive force (SMF) than the PMF and pH value in the medium without interfering with other cellular processes, this chimeric motor has become a favorable target in recent BFM studies (16-18).

To clarify the working mechanism of the flagellar motor, we need to understand the mechanochemical cycle of torque generation and how it is coupled to ion flux. In the past three decades, various experimental techniques have been implemented in the study of BFM. Before direct step measurement, the torque-speed relationship was the major biophysical probe to study the mechanism. By attaching a polystyrene bead onto the flagellum, or by applying rotating electric field, Berg and coworkers, followed by other researchers, measured how the motor torque (output of the motor) varies with speed (16, 18-24). The experiments can be viewed as early experimental efforts of biophysics studies at single protein/protein complex levels. It gives a full picture of the motor's output under external loads, and gives an indication of the energy conversion efficiency. The observed motor torque-speed relations, which show sharp transitions (the "knee") between a plateau region at low speed and a steep concave-down region at high speed, remained unexplained for a long time (1).

In our previous paper, we constructed a mathematical model to explain the observed motor torque-speed relationship (25). We showed that the flat plateau and knee are mainly due to the following facts: 1) rotation is observed through a soft elastic linkage between the motor and the viscous load; 2) the diffusion dynamics of the load and the internal kinetics of the motor are on different time scales. Our model suggested that motor dynamics in the plateau region and in the concave-down region is controlled by thermodynamics and internal motor kinetics, respectively. Consequently, we suggested that the two components of the ion motive force, the membrane potential and the transmembrane ion gradient, are equivalent in controlling motor speed in the plateau region, but may be non-equivalent in the concave-down region. The latest experiment by Lo *et al.* confirmed that individual components of the SMF show non-equivalent influence on the chimera motor function in the low load regime (26).

Our model also predicted that the motor speed at vanishing load (the zero-load speed) decreases with the number of stators. However, recent experiment by Yuan and Berg showed the zero-load speed is independent of the stator number (27). They performed numerical simulations with our model, and stated that the experimental result can be recovered if the stator springs, neglected in our original work, are explicitly treated and are sufficiently soft. However, this raises another concern about the model. One expects that a motor with soft stator springs does not show clear steps (28). On the other hand, Sowa *et al.* observed clear 26 steps per revolution in a slow rotating chimera motor. In this work, we examine our model if it is compatible with both the zero-load speed experiment and the stepping experiment. We focus on the dynamics of the flagellar motor. We first improve the modeling of ion hopping on/off rates in the model by explicitly considering extracellular/intracellular ion concentration. This modification allows separate treatment of the membrane potential and the ion gradient. We present results that can fit *E. coli* and chimera motor data respectively. Models of the two types of motor are derived from the same framework but differ in the values of some parameters (e.g, ion hopping rates). Next, we show that the model predicts that the flagellar motor is a stepping motor and discuss the corresponding dwelling time distribution. After we introduce a soft stator spring in the model, the model reproduces both the stepping behavior and the correct zero-load speed dependence on the stator number. We further discuss the stepping behavior when two stators are engaged in the system. A series of testable predictions are made, which will become the starting point of a new generation of experiments.

## MODEL FORMATION AND COMPUTATIONAL DETAILS

With extensive biochemical, Cryo-EM, crystallography, and mutational studies, detailed information of the motor has been accumulated. Current biochemical and structural studies imply that the motor torque is generated by stator conformational changes upon ion binding/unbinding to the negatively charged D32 residue on the MotB helices (D24 on PomB for the $Na^+$ motor). This motion is transmitted to the rotor via interactions at the rotor-stator interfaces (see 1, 7, and references therein). Details of these interactions will remain vague until the atomic structure of the stator has been determined; currently the structures of but a few portions of the rotor are available (29-31).

Our coarse-grained model integrates available information from various experimental observations (25). In order to generate sufficient torque, we assume that one torque generation cycle of the stator is driven by the free energy derived from transporting two periplasmic protons to the two negatively charged D32 residues on the two MotB helices, then to the cytoplasm. On binding and releasing the ions, two cytoplasmic MotA loops alternate in contacting successive FliGs on rotor, like two alternating "pistons". The MoA loop motions result in a downward stroke followed by a recovery stroke, each of which pushes the rotor to rotate. During the cycle, the stator is always engaged with the rotor; i.e. the duty ratio is 1. The binding energy of the protons to MotB is converted into a 'flashing' electric field in the stator that triggers a pair of conformational transitions (Fig. 1b). The torque thus generated is transmitted to the rotor when the MotA loops are in contact with the FliGs. The interaction between MotA and FliG is most likely (but not necessarily) dominated by electrostatic and steric interactions (13, 25). Detailed modeling of these interactions has to wait for more structural information.

The above process can be described mathematically by a set of stochastic equations. The dynamics of the single stator motor pulling a viscous load via an elastic linkage can be described by the Langevin equation:

$$\text{Rotor}: \underbrace{\zeta_R \frac{d\theta_R}{dt}}_{\substack{\text{Viscous drag torque}\\ \text{on the rotor}}} = \underbrace{-\frac{\partial}{\partial\theta_R} V_{RS}\left(s,\theta_R-\theta_S\right)}_{\substack{\text{Rotor-Stator}\\ \text{interaction force}}} - \underbrace{\kappa\left(\theta_R-\theta_L\right)}_{\substack{\text{Elastic coupling}\\ \text{force}}} + \underbrace{\sqrt{2k_BT\zeta_R}\, f_R(t)}_{\substack{\text{Brownian torque}\\ \text{on the rotor}}} \qquad (2)$$

where the angle $\theta_S, \theta_R$ and $\theta_L$ are defined in Figure 1c, and $\theta_S$ is set to zero except in simulations that consider stator spring explicitly. $\zeta_R$ is the effective drag coefficient of the rotor. The viscous load (e.g., the polystyrene bead) is coupled to the rotor via an elastic linkage, which is modeled by a harmonic potential, $V_{RL} = 1/2\kappa(\theta_R - \theta_L)^2$. The last term is the stochastic Brownian force acting on the rotor, where $f_R(t)$ is uncorrelated white noise with normal Gaussian distribution (32, 33). $V_{RS}$ is the potential of mean force of the rotor-stator interaction, and *s* is a binary variable referring to the stator conformational state: right or left piston down. The potentials $V_{RS}$ are chosen as identical periodic free energy profiles, each offset by a half-period, as shown in Figure 1b. The choices of the potential shapes and the exact half-period offset here are for simplicity, and can be improved when more structural and dynamic information is available. Our numerical studies have found that our conclusion does not depend upon the exact shape of the potentials. The slope of $V_{RS}$ determines the force profile the stator exerts on the rotor. The high peak at the top of each potential ensures tight-coupling between the rotor and stator by preventing a thermal fluctuation from carrying the system to the left (backward slipping) and 'wasting' a pair of translocated protons. The structural correspondence of the barrier needs further study. We suggest that steric interactions between FliGs and the cytoplasmic loop of MotA may serve the role. In parallel to the motor spatial motion, a stator can switch between the two stator chemical states, which correspond to switching between the two potential curves shown in Figure 1b. The switching is described by Kramers jump processes between the two potential curves. The Kramers rates are directly related to the ion motive force (IMF). In our original model, the effect of IMF was described by a composite factor. To study the effect of the two components (ion concentration gradient and transmembrane potential) separately, in this work we model the jump rates for the exchange of 2 ions between the periplasm and stator binding sites as:

$$k_{on}^{peri} = f(\theta_R - \theta_S, \alpha_1, \beta_1)(C_{peri})^2 k_0 \exp(0.5(V_1 - V_2 + 2\gamma e\Delta\psi)/k_B T) \tag{3}$$

$$k_{off}^{peri} = f(\theta_R - \theta_S, \alpha_1, \beta_1)\exp(-2pK_a)\ k_0 \exp(-0.5(V_1 - V_2 + 2\gamma e\Delta\psi)/k_B T) \tag{4}$$

and those between the cytoplasm and a stator binding sites as,

$$k_{off}^{cyto} = f(\theta_R - \theta_S, \alpha_2, \beta_2)\exp(-2pK_a)k_0 \exp(0.5(V_2 - V_1 + 2(1-\gamma)e\Delta\psi)/k_B T) \tag{5}$$

$$k_{on}^{cyto} = f(\theta_R - \theta_S, \alpha_2, \beta_2)(C_{cyto})^2 k_0 \exp(-0.5(V_2 - V_1 + 2(1-\gamma)e\Delta\psi)/k_B T) \tag{6}$$

where the functions $V_1$ and $V_2$ refer to the potentials $V_{RS}$ for the two stator states (empty and occupied, respectively), $C_{peri}$ and $C_{cyto}$ are the ion concentrations at the periplasmic and cytoplasmic sides, respectively, in units of mM. $pK_a$ is the intrinsic dissociation constant of the ion binding site along the stator channel. $k_0$ is a prefactor of the transition rates. The function $f(\theta,\alpha,\beta)$ is the transition window accounting for the requirement that chemical transitions and the rotor position are coupled (see ref (25) for details). Here we use a triangle shape

$$f(\theta,\alpha,\beta)=\begin{cases}\dfrac{\theta-\alpha}{\frac{1}{2}(\beta-\alpha)}, \text{ for } \alpha<\theta<\frac{1}{2}(\alpha+\beta)\\ 1-\dfrac{\theta-\frac{1}{2}(\alpha+\beta)}{\frac{1}{2}(\beta-\alpha)}, \text{ for } \frac{1}{2}(\alpha+\beta)<\theta<\beta\\ 0, \text{ otherwise}\end{cases} \tag{7}$$

or a uniform function

$$f(\theta,\alpha,\beta)=\begin{cases}1, \text{ for } \alpha<\theta<\beta\\ 0, \text{ otherwise}\end{cases} \tag{8}$$

In each torque generation cycle, two ions from the periplasm jump onto a stator and are later released to the cytoplasm. The rotor rotates an average angle of 2π/26, and the free energy of the overall systems drops $-k_B T\ln\left(\dfrac{k_{on}^{peri}}{k_{off}^{peri}}\dfrac{k_{off}^{cyto}}{k_{on}^{cyto}}\right)=-2e\Delta\tilde{\mu}$. Therefore, in the above rate expressions detailed balance is automatically satisfied. For simplicity we assume that ion binding is cooperative. Notice that the two components of the ion motive force affect the jump rates differently. The ion concentrations affect only the on rates. The effect of the membrane potential is more complicated, and may be due either to increasing local ion concentrations at the membrane surface or affecting the transition dynamics directly. Here for simplicity we assume that the on- and off- rates for a particular jump are equally affected by the membrane potential. The parameter γ specifies the partition of membrane potential for the two half steps of the torque generation cycle. We found a γ value ~ 0.6 gives the best fit to the results of Lo *et al* (26). This result is consistent with the structural fact that the residue D32 resides close to the cytoplasmic end of the membrane, and thus one expects a larger effect of the membrane potential on the ion hopping rates from the periplasmic side.

The next step in our model is to include the load, e.g. the latex bead attached to the flagellum. Simultaneously, the motion of the load is described by the Langevin equation:

$$\text{Load}: \underbrace{\zeta_L\frac{d\theta_L}{dt}}_{\text{Viscous drag force on the Load}}=\underbrace{\kappa\left(\theta_R-\theta_L\right)}_{\text{Elastic coupling force}}+\underbrace{\sqrt{2k_BT\zeta_L}f_L(t)}_{\text{Brownian force on the load}} \tag{9}$$

Here the elastic coupling term appears with sign opposite that in Eq. (2), and $\zeta_L$ is the drag coefficient of the load. The last term is the Brownian force on the load. The characteristic time scale for the motion of the load is $t_L = \zeta_L/\kappa$.

The model equations (2) and (9) can be replaced by the equivalent coupled Fokker-Planck equations with $\theta_S = 0$, describing the probability density, $\rho_j(\theta_L, \theta_R, t)$ of the rotor and load being at position $(\theta_L, \theta_R)$ and chemical state $j$ at time $t$ while driven by a single stator:

$$\frac{\partial \rho_j}{\partial t} = \underbrace{\frac{1}{D_R}\frac{\partial}{\partial \theta_R}\left(\frac{1}{k_B T}\left(\kappa(\theta_L - \theta_R) + \frac{\partial}{\partial \theta_R} V_j\right)\rho_j\right) + \frac{1}{D_L}\frac{\partial}{\partial \theta_L}\left(\frac{1}{k_B T}\kappa\left(\theta_R - \theta_L\right)\rho_j\right)}_{\text{Motion due to the potential and the load force}}$$

$$+ \underbrace{D_R \frac{\partial^2 \rho_j}{\partial \theta_R^2} + D_L \frac{\partial^2 \rho_j}{\partial \theta_L^2}}_{\text{Brownian motion}} + \underbrace{\sum_i k_{ji}\left(\theta\right)\rho_i}_{\text{Chemical transitions}}, \quad j = 1,2 \qquad (10)$$

Here $D_R$ and $D_L$ are the diffusion constants of the rotor and the bead, respectively, related to the drag coefficients by the Einstein relation, $\zeta = k_B T/D$. We solved the steady state of the Fokker-Planck equations with the algorithm developed by Xing *et al* (34). The algorithm discretizes the conformational coordinates, and transforms the partial differential equations into a jumping process over many discrete states with their normalized populations $p$ (defined as the probability density integrated over the discrete regions) described in the form Kp = 0. The composite K matrix contains transitions along both the conformational and reaction coordinates (see ref (35) for details). The steady state motor rotation rate is obtained by calculating the spatial flux (summing over all the chemical states) at one spatial point. We also performed Langevin dynamics simulations with one or two stators engaged to obtain single motor trajectories.

More degrees of freedom need to be included if we consider the stator fluctuations. Structural studies show that the stators are fixed to the peptidoglycan through elastic linkages (2, 36). In our previous study, we neglected the stator fluctuations for mathematical simplicity. Recent experiments by the Berg group revealed that stator fluctuations give rise to some new dynamic behaviors in the low-load region (27). Their results contradict a prediction of our original model (25). These researchers showed that the experimental results can be reproduced if the stator springs are included in our model. In some results presented here, we modeled the stator linkages by harmonic springs and allowed the stators to fluctuate around their equilibrium position. Similar to Eq. (2) and Eq. (9), the movement of each stator can be described by an additional Langevin equation.

$$\text{Stator}: \underbrace{\zeta_{Si}\frac{d\theta_{Si}}{dt}}_{\substack{\text{Viscous drag torque}\\ \text{on the stator}}} = \underbrace{\frac{\partial}{\partial\theta_{Si}} V_{RSi}\left(s,\theta_R-\theta_{Si}\right)}_{\substack{\text{Rotor-Stator}\\ \text{interaction force}}} - \underbrace{\kappa_S\left(\theta_{Si}-\theta_{0i}\right)}_{\substack{\text{Elastic coupling}\\ \text{force}}} + \underbrace{\sqrt{2k_BT\zeta_S}\, f_{Si}(t)}_{\substack{\text{Brownian torque}\\ \text{on the stator}}} \tag{11}$$

where $\theta_{Si}$, $\theta_{0i}$, and $S_i$ are the position, equilibrium position, and the ion occupation state of the *i*-th stator. When there are N stators functioning in the system, the torque applied to the rotor is a sum of the interaction potential induced by each individual stator at different position and with different ion binding status. Correspondingly, the rotor-stator interaction term in Eq. (2) becomes:

$$\text{Rotor-Stator interaction force} = -\frac{\partial}{\partial\theta_R}\left(\sum_{i=1}^{N} V_{RSi}(s_i,\theta_R-\theta_{Si})\right) \tag{12}$$

The complete BFM model with stator springs explicitly treated is solved by the Langevin simulation approach. In these simulations, we implemented parallel Monte Carlo processes, to simulate the motion of the rotor, stators, and the bead driven by model potentials and to determine the ion hopping on/off in each stator. The motor speed is obtained by running a very long time simulation and dividing the final displacement by the total simulation time. In our current model, stators interact indirectly with each other through working against a common rotor. Langevin simulations are also used to study the stepping behavior of the motor. The stepping statistics (e.g. stepsize and dwelling time distribution) are collected by a step finder program, which is described in ref.(37). The same program was previously used to analyze the BFM stepping data (17).

# RESULTS

## 1) Torque-speed relationship and effects of different energy components

First we reproduce the *E. coli* BFM torque speed curve with the new jumping rate formulation. Under normal living conditions, the *E. coli* BFM functions with intracellular pH 7.6, external pH 7, and membrane potential 120 mV. Without modifying the potential profiles, the *E. coli* BFM torque speed curve can be easily reproduced by inputting these realistic values into our new formulation (Fig. 2a). Model parameters are given in Table 1.

The chimera motor uses a $Na^+$ type BFM stator and $H^+$ type BFM rotor. The torque speed relationship of the chimera motor has been reported by Inoue *et al.* (18). It is highly similar to that of the *E. coli* BFM except for a higher 'knee' speed and zero-load speed. Without changing the driving potential profiles, we substitute the experimental values of chimera motor living condition into our model and fit the chimera torque speed curve. In Fig. 2b we present two model results, one with the same chemical transition window as that of *E. coli* motor and the other one with a uniform window. Because the torque-speed curves can be reproduced (on both *E. coli* and chimera) with the same model framework, there is likely no fundamental distinction in the energy transduction mechanism between *E. coli* and chimera motors. The difference in the detailed shapes of the motor torque-speed relations may reflect subtle structural differences. We model the difference by the transition window shape, which reflects the coupling between stator ion transduction and the relative positions of rotor and stator.

Our model gives an explicit answer to the mysterious BFM torque-speed relationship. At high load, the bead response time is much longer than the motor internal (ion hopping on/off and rotor motion) dynamics. The motor dynamics is near equilibrium under external constraint (from the load). The motor torque is determined by thermodynamics (25, 38-40).

$$\zeta_L \omega_L \approx \Delta G/\delta = (\Delta H - T\Delta S)/\delta. \tag{13}$$

where $\omega_L$ is the angular velocity of the load, $\delta = 2\pi/26$ is the angular step length (i.e. distance between FliGs), and $\Delta G$ is the free energy drop per stator cycle derived from IMF(PMF or SMF). However, at low load, there is no time scale separation between the bead relaxation and the internal motor processes, and the motor dynamics is kinetics-controlled. The observed transition between the plateau and knee region is quite sharp. As discussed in our previous paper, this observation can be explained through interplay between localized transitions along $\theta_R$ and stator mutual interference. To make a transition from one potential curve to another one (corresponding to ion hopping on and off within one stator), the rotor needs to rotate into the transition window. However, other stators may push the rotator to move out of the transition window before the chemical transition takes place. Consequently, the rotor is trapped before thermal fluctuations bring it back into the transition window so the stator can switch its chemical state. A load reduces occurrence of the trap by pulling the rotor backward. Therefore decreasing the load shortens the bead response time, and lengthens the motor internal dynamics at the same time. This results in abrupt change of the system from the thermodynamics-controlled plateau region (with time-scale separation between the bead response time and the motor internal kinetics) to the kinetics-controlled knee region (with no time-scale separation between them).

A direct prediction of the above discussion is that the two components of the ion motive force, the concentration gradient, and the transmembrane potential, are equivalent in the high-load region, but may not necessarily be equivalent in the low-load region. Figure 3a shows that the motor speed is proportional to the membrane voltage in both directions. This result is consistent with Berg's experiment (22, 23). However, as shown in Figure 3b, the motor speed responds to periplasmic ion concentrations asymmetrically, and becomes saturated at high ion concentrations, consistent with experimental observations (16).

With our model we can also investigate the effect of varying the relative ion concentration and membrane potential contributions while holding the total IMF constant. Figure 3c shows that the external ion concentration has much stronger influence on the motor output. The motor speed decreases dramatically when external ion concentration is lowered, despite the total IMF being compensated by a transmembrane voltage increase. Figure 3c compares our simulations with the experimental observation of Lo *et al.*(26). Therefore, our model correctly predicts that the motor speed depends more strongly on the external ion concentration than on the membrane voltage. One obvious explanation is that the diffusion limited binding of ions is the rate limiting step at low load, but not at high load.

## 2) Zero-load speeds and the stator springs

Our original model predicted that the motor zero-load speed (i.e., the rotation speed without external load) decreases with the number of stators engaged, a remnant of the stator mutual interference effect discussed above (25). Recently, Yuan and Berg tested this prediction in a proton-driven motor (27). Their observations show that the zero-load speeds with different numbers of stators converge to a single value. This result suggests that the mutual interference between stators is not as strong as we suggested near the zero-load regime. This can be explained by the fact that MotB in each stator is linked to the peptidoglycan through α-helices several nanometers long. The linker may introduce compliance and allow lateral fluctuation of the stator. In our original model, we neglected such stator fluctuations due to the stator springs. Yuan and Berg performed numerical simulations using our model, and found a converged zero-load speed can be obtained by introducing soft stator springs. With the stator springs, the above mentioned destructive interference among stators at high speed is reduced (see Figure 7c). We performed similar simulations (Fig. 4), and found that a spring stiffness constant ~ 200 pNnm/rad$^2$ is sufficient to reasonably reproduce the experimental data. The angular spring constant corresponds to a translational spring constant 1 pN/nm if we assume the rotor radius is 15 nm. This value agrees well with the estimated linker stiffness assuming it is $\alpha$-helix and with the value determined by Yuan and Berg (27).

### 3) The motor is a stepper

As discussed above, the zero-load speed results require lateral fluctuations of the stators. However, existence of soft stator springs can smear the steps in a motor trajectory (28). On the other hand, steps have been observed experimentally for the chimera motor. Can our model reproduce both sets of experiments? Below we show some model simulation results following experimental conditions and the methods used to analyze the experimental data.

Similar to the experimental procedure, in our simulation we assign $N_{stator} = 1$ and lower the external sodium concentration. Stepping behavior becomes obvious when the motor speed is lower than 10 Hz. In Fig. 5a, we show a series of stepping traces under various external sodium concentrations. Notice that in the experimental traces (Fig. 5b) published by Sowa *et al.*, the information of the external sodium concentration is lacking. By comparing the experimental traces with our simulation, we can make an educated guess of the external sodium concentration of the cells being studied in these experiments. For example, the central three traces running at 0.5 ~ 2 Hz are from an environment with approximately 0.5 ~ 1.5 mM external sodium concentration. If the external sodium concentration is lower than 0.5mM, backwards steps occur frequently and the motor can not make noticeable advancement.

It remains to be confirmed if steps can be resolved in wild-type *E. coli* motors as in chimera motors. Next we theoretically explore the conditions under which *E. coli* motor stepping can be seen. The speed of the motor decreases rapidly when the external pH value is increased. However, in real experiment the *E. coli* cells are not able to endure a large pH change since they cannot survive a strong alkali environment. Therefore, our aim is to find the least demanding condition under which steps can be resolved. Figure 6a shows simulated results with pH external = 8.4 and pH internal = 7.6. Two stator spring constants are used. One is $\kappa = 200$ pN nm/rad$^2$, the value used above to reproduce the zero-load speeds; another is $\kappa = 3000$ pN nm/rad$^2$. We suggest that the spring constant could be stiffened *e.g.* through antibody binding onto the stator linker or use of a mutant with a shorter and thus presumably stiffer linker. The motor runs at about 8 Hz with detectable steps in both cases, although the trajectory with the softer stator spring is noisier. Figure 6b shows the step-size distribution obtained with the step finder algorithm used previously (37). The step-size distribution is centered around 26 steps / revolution, consistent with the experimental result of Sowa *et al* (17) for the chimera motor. In our model, each motor cycle has two half steps. However, under the experimental conditions simulated in Figure 6b only the ion binding from the periplasm is rate-limiting: the second half-step corresponding to release of two ions into the cytoplasm follows the first half-step too rapidly to be resolved. Our model suggests that clear substeps may be observed if the ion binding sites (D32) have higher ion binding affinity than that of the wild type, and thus lower ion off rate. Figure 6c shows the corresponding dwelling time distributions. It can be fitted with single exponential decay. Recent higher resolution experimental results show similar results (unpublished data in R. Berry's lab).

To conclude, our model reproduces the chimera motor stepping, and predicts the conditions under which *E. coli* motor stepping should be observable, and the corresponding statistics. Experimental realization of these conditions is on the way.

The motion of a protein motor is continuous for all biological purposes. Why does the continuous motion of the motor result in stepping behavior? Stepping behavior has been observed for many protein motors (41, 42). Figure 5c schematically shows how the continuous motion of a protein motor produces steps. For most of the time, the motor fluctuates around a potential minimum, so one observes the motor (or the indicator) to fluctuate around a fixed angular (or spatial) position (labeled 1). The distribution of the motor position reveals the local structure of the potential well. After a chemical transition takes place, the motor slides down a new potential until it reaches the next potential minimum. Experimentally one observes fast motion of the motor (labeled 2) followed by fluctuation around the new minimum. The relatively fast transient motion and long time dwelling around some positions give the stepping behavior of the motor, and justifies usage of discrete kinetic models on modeling protein motors (43).

Occasionally backward steps can be observed. Two possible transitions can result in backward motion. The motor, with the ion binding sites empty or occupied, may simply slip backward over the potential barrier (labeled 3). In this case ions are translocated without net motor motion, thus the two motions are decoupled. The backward step could also be the inverse of the process described by step 2 (labeled 4). A motor rests in a state with empty stator binding sites and angular positions that ions are accessible to the binding sites from the periplasmic side (the "PE" state in a discrete kinetic model). Random thermal fluctuations allow the motor to rotate to the angular locations that the stator binding sites are accessible from the cytoplasmic side (the "CE" state). Then the motor picks up a pair of ions (the "CO" state), fluctuates back ("CO" → "PO"), and releases ions to the periplasmic side ("PO" → "PE"). In this case the motor motion and the chemical transition are still tightly coupled. The BFM functions as a pump when this type of backward steps takes place. One difference between these two mechanisms is that the loose-coupling mechanism produces a full backward step only, but the tight coupling mechanism can in principle produce half steps. The backward sub-steps, if exist, may also be resolved if a mutant with the stators having high ion binding affinity is used, so the step of releasing the binding ions to the periplasm can be slowed down. Decreasing the extracellular ion concentration has less effect on the loose-coupling mechanism than on the tight-coupling mechanism. For the latter a longer waiting time for the motor to pick up ions from the periplasm increases the probability that the motor instead pick up ions from the cytoplasm and a backward step takes place. It is experimentally observed that the number of backward steps increases on decreasing the extracellular ion concentration. This suggests that the tight-coupling backward mechanism contribute to the observed backward steps. However, we cannot rule out the loose-coupling mechanism. We want to point out that description of backward motion is automatically included in a potential based continuous model (35).

### 4) Step size vs. stator number

In this section we discuss the stepping behavior for a motor with multiple stators engaged. Fluctuation analysis predicted that the step-size decreases to 1/n of δ if there are n stators in the system (44, 45). However, recent experiment on the chimera motor reveals 'the apparent independence of step size on stator number' (17). These two results obviously contradict with each other.

In stator resurrection experiments using the chimeric motor, one decreases the external ion concentration to disengage the stators from the rotor, then waits for the stators to resurrect, *i.e.*, re-engage one by one in random sequence (17). Therefore the relative distance between the two resurrecting stators may be different on different experimental attempts. Because our model potentials are $2\pi/26$ periodic, we can project all the stator positions into one period $\delta=2\pi/26$. The projection allows us to visualize the relative phase of these stator positions. For simplicity, here we only discuss $N_{stator} = 2$. Taking the first stator as the reference point, the second stator can be bound at any position $\Delta\theta_S \in [0, \delta]$. Figure 7 gives a qualitative picture of the stepping behavior of a motor with two stators based on our model framework. Figure 7 a and b show two cases with stiff stator springs but different ratios of the stator distance $\Delta\theta_S$ over the rotor periodicity $\delta$ ($2\pi/26$). If the ratio is not integer, one expects doubled step numbers and smaller step sizes reflecting $\Delta\theta_S/\delta$ compared to the one-stator case. If the ratio is integer, around each dwelling configuration (one local minimum of the composite potential) the system cannot move forward until both the stators change their chemical states. Consequently, the step numbers and size are the same as in the one-stator case, but with longer dwelling time on average. With soft stator springs, the spatial mutual coupling between the chemical transitions within the stators is reduced (Figure 7c). The above discussed difference with different $\Delta\theta_S / \delta$ may be less clear. Figure 8 shows the step size distributions calculated from simulated traces by the step finder with different values of the stator spring stiffness and $\Delta\theta_S / \delta$. With stiff stator springs, and $\Delta\theta_S / \delta = 0.5$ or 1, the step sizes are indeed centered around $0.5\ \delta$ and $\delta$, respectively (with longer average dwelling time for the latter, results not shown). With soft stator springs, on the other hand, in both cases the step sizes show broad distributions centered around $\delta$. The soft stator spring results may explain why the observed step sizes are apparently independent of stator number. The fluctuation analysis of Samuel and Berg(44) counts the number of statistically independent rate-limiting events, which are not necessarily the same as observable mechanical steps.

## DISCUSSIONS AND CONCLUSIONS

Our model is a work in progress, which can be refined in several aspects in response to future experimental results:

First, in our original model, the stator effect is partly absorbed in the model parameters (parameter renormalization). With explicit treatment of the stator springs, the model needs to be re-parameterized. Our numerical studies found that the generic behaviors of the torque-speed curves, i.e, existence of plateau and linear ion motive force dependence of the rotation speed at low speed region, and decline of the motor torque at high speed region, are to a large extent insensitive to model parameters (see also Figure 4). As explained in the original paper, they are a general consequence of the interplay of several times scales in the system. On the other hand, detailed shapes of the torque-speed curves do depend on some model parameters. The stator springs greatly expand the degrees of freedom in the model. An efficient numerical method is needed for fast parameter optimization in the future.

Second, the model discussed in the original paper and in this work is rather generic. Some details relevant to the motor function may be missing. Currently we assign all the stator-stator interactions through a common rotor. The neighboring stators may interact directly as well as through the rotor. A similar idea has been proposed for the $F_1$ part of the ATP synthase (46). For the flagellar motor, EM images show that the arrangement of stators is crowded (47). A stator under tension distorts the membrane as well as the stator springs. The stators may interact with each other through tension-dependent membrane-mediated interactions (48). This lateral coupling may assure sufficient destructive stator mutual interference to produce the sharp transition of the motor torque-speed curves, and that the mutual interference drops on decreasing the load to produce the correct zero-load speed behavior.

Third, in our model we enforce the tight coupling assumption by high potential barriers. The assumption means that there is a definite coupling between rotor rotation and the number of ions transferred: one step ($\sim 2\pi/26$) of forward rotation of the rotor accompanies transferring two ions from the periplasm to the cytoplasm; one step of backward rotation of the rotor accompanies transferring ions from the cytoplasm to the periplasm (therefore the BFM acts as a pump). We made this assumption because several experimental results are in agreement with the consequences if the motor is tightly coupled. However, none of the existing experimental evidence really precludes the possibility that the motor is not perfectly coupled (*i.e.*, near 100%). To clarify this problem, we require an accurate measurement of the stall torque and the corresponding stepping statistics in single-stator motors at both high load and low load. Then, the exact number of ions consumed in a motor step can be calculated. Furthermore, if one can measure and control the ion flux through the stator channel, the answer to the above ‘coupling’ puzzle will be straightforward.

In summary, we analyzed the dynamics of our BFM model in detail. The model predicts the observed non-equivalence of the two components of the ion motive force at high speed regions. With explicit consideration of the stator springs, the model reproduces the observed zero-load speed dependence on stator numbers. The motor can be a stepper even in the presence of stator springs. With two stators engaged, however, smaller steps are difficult to resolve. We suggest that if the stator springs can be stiffened (e.g., through antibody binding), more insights into the BFM dynamical behaviors can be obtained. We also suggest that sub-steps (for both forward and backward steps) may be resolved if one uses a mutant with the stator charges having higher affinity for the binding ions than the wild type does.

## ACKNOWLEDGEMENTS

F.B. is supported by the Wellcome Trust VIP research funding. C.-J. L thanks the Swire Group/ORS for financial support. J. X. was initially supported by a Lawrence Livermore National Laboratory Directed Research and Development grant. This work was partly performed under the auspices of the U.S. Department of Energy by the University of California, Lawrence Livermore National Laboratory under Contract No. W-7405-Eng-48.

## REFERENCES

1. Berg, H. C. 2003. The Rotary Motor of Bacterial Flagella. Annu. Rev. Biochem. 72:19-54.
2. Blair, D. F., D. Y. Kim, and H. C. Berg. 1991. Mutant MotB proteins in Escherichia coli. J.Bacteriol. 173:4049-4055.
3. Berg, H. C. 2003. The bacterial rotary motor. In The enzymes: Energy coupling and molecular motors. F. Tamanoi, and D. D. Hackney, editors. Academic Press. 468.
4. Berry, R. 2004. The Bacterial Flagellar Motor. In Forces, Growth and Form in Soft Condensed Matter: At the Interface between Physics and Biology. A. Belushkin, editor. Kluwer Academic, The Netherlands. 145-164.
5. Berg, H. C. 1974. Dynamic properties of bacterial flagellar motors. Nature 249:77-79.
6. Reid, S. W., M. C. Leake, J. H. Chandler, C. J. Lo, J. P. Armitage, and R. M. Berry. 2006. The maximum number of torque-generating units in the flagellar motor of Escherichia coli is at least 11. Proc. Natl. Acad. Sci. USA 103:8066-8071.
7. Blair, D. F. 2003. Flagellar movement driven by proton translocation. FEBS Letters 545:86-95.
8. Sowa, Y., and R. M. Berry. 2008. Bacterial flagellar motor. Quart. Rev. Biophys. 41:103-132.
9. Thomas, D. R., N. R. Francis, C. Xu, and D. J. DeRosier. 2006. The three-dimensional structure of the flagellar rotor from a clockwise-locked mutant of Salmonella enterica Serovar Typhimurium. J. Bacteriol. 188:7039-7048.
10. Marlovits, T. C., T. Kubori, A. Sukhan, D. R. Thomas, J. E. Galan, and V. M. Unger. 2004. Structural Insights into the Assembly of the Type III Secretion Needle Complex. Science 306:1040-1042.
11. Zhai, Y. F., W. Heijne, and J. Saier, Milton H. 2003. Molecular modeling of the bacterial outer membrane receptor energizer, ExbBD/TonB, based on homology with the flagellar motor, MotAB. Biochim. Biophys. Acta 1614:201-210.

12. Cascales, E., R. Lloubes, and J. N. Sturgis. 2001. The TolQ-TolR proteins energize TolA and share homologies with the flagellar motor proteins MotA-MotB. Mol. Microbiol. 42:795-807.
13. Zhou, J., S. A. Lloyd, and D. F. Blair. 1998. Electrostatic interactions between rotor and stator in the bacterial flagellar motor. Proc. Natl Acad. Sci. USA 95:6436.
14. Yorimitsu, T., and M. Homma. 2001. $Na^+$-driven flagellar motor of *Vibrio*. Biochim. Biophys. Acta 1505:82-93.
15. Asai, Y., I. Kawagishi, R. E. Sockett, and M. Homma. 1999. Hybrid Motor with H+- and Na+-Driven Components Can Rotate Vibrio Polar Flagella by Using Sodium Ions. J. Bacteriol. 181:6332-6338.
16. Sowa, Y., H. Hotta, M. Homma, and A. Ishijima. 2003. Torque-speed Relationship of the $Na^+$-driven Flagellar Motor of Vibrio alginolyticus. J. Mol. Biol. 327:1043-1051.
17. Sowa, Y., A. D. Rowe, M. C. Leake, T. Yakushi, M. Homma, A. Ishijima, and R. M. Berry. 2005. Direct observation of steps in rotation of the bacterial flagellar motor. Nature 437:916-919.
18. Inoue, Y., C.-J. Lo, H. Fukuoka, H. Takahashi, Y. Sowa, T. Pilizota, G. H. Wadhams, M. Homma, R. M. Berry, and A. Ishijima. 2008. Torque-speed relationships of Na+-driven chimeric flagellar motors in Escherichia coli. J. Mol. Biol. 376:1251-1259.
19. Chen, X., and H. C. Berg. 2000. Solvent-isotope and pH effects on flagellar rotation in *Escherichia coli*. Biophys. J. 78:2280-2284.
20. Berg, H. C., and L. Turner. 1993. Torque generated by the flagellar motor of Escherichia coli. Biophys. J. 65:2201-2216.
21. Ryu, W., R. Berry, and H. Berg. 2000. Torque-generating units of the flagellar motor of *Escherichia coli* have a high duty rotio. Nature 403:444-447.
22. Gabel, C. V., and H. C. Berg. 2003. The speed of the flagellar rotary motor of escherichia coli varies linearly with protonmotive force. Proc. Natl. Acad. Sci. USA 100:8748-8751.
23. Fung, D., and H. C. Berg. 1995. Powering the flagellar motor of *Escherichia coli* with an external voltage source. Nature 375:809-812.
24. Chen, X., and H. C. Berg. 2000. Torque-speed relationship of the flagellar rotary motor of Escherichia coli. Biophys. J. 78:1036-1041.
25. Xing, J., F. Bai, R. Berry, and G. Oster. 2006. Torque-speed relationship for the bacterial flagellar motor. Proc. Natl. Acad. Sci. USA 103:1260-1265.
26. Lo, C.-J., M. C. Leake, T. Pilizota, and R. M. Berry. 2007. Nonequivalence of membrane voltage and ion-gradient as driving forces for the bacterial flagellar motor at low load. Biophys. J. 93:294-302.
27. Yuan, J., and H. C. Berg. 2008. Resurrection of the flagellar rotary motor near zero load. Proc. Natl Acad. Sci. USA 105:1182-1185.
28. Walz, D., and S. R. Caplan. 2005. A kinetic and stochastic analysis of crossbridge-type stepping mechanisms in rotary molecular motors. Biophys. J. 89:1650-1656.
29. Lloyd, S., F. Whitby, D. Blair, and C. Hill. 1999. Structure of the c-terminal domain of FliG, a component of the rotor in the bacterial flagellar motor. Nature 400:472-475.
30. Brown, P., C. Hill, and D. F. Blair. 2002. Crystal structure of the middle and C-terminal domains of the flagellar rotor protein FliG. EMBO J. 21:3225-3234.
31. Brown, P., M. Mathews, L. Joss, C. Hill, and D. F. Blair. 2005. Crystal Structure of the Flagellar Rotor Protein FliN from *Thermotoga maritima*. J. Bacteriol. 187:2890–2902.
32. Risken, H. 1996. The Fokker-Planck Equation: Methods of solutions and applications. Springer-Verlag, New York.

33. Zwanzig, R. 2001. Nonequilibrium Statistical Mechanics. Oxford University Press, Oxford.
34. Xing, J., H.-Y. Wang, P. Dimroth, C. von Ballmoos, and G. Oster. 2004. Torque generation by the $F_o$ motor of the sodium ATPase. Biophys. J. 87:2148-2163.
35. Xing, J., H.-Y. Wang, and G. Oster. 2005. From continuum Fokker-Planck models to discrete kinetic models. Biophys. J. 89:1551-1563.
36. Muramoto, K., and R. M. Macnab. 1998. Deletion analysis of MotA and MotB, components of the force-genearting unit in the flagellar motor of Salmonella. . Mol. Microbiol. 29:1191-1202.
37. Kerssemakers, J. W. J., E. Laura Munteanu, L. Laan, T. L. Noetzel, M. E. Janson, and M. Dogterom. 2006. Assembly dynamics of microtubules at molecular resolution. Nature 442:709-712.
38. Astumian, R. D., and I. Derenyi. 2001. Towards a chemically driven molecular electron pump. Phys. Rev. Lett. 86:3859-3862.
39. Elston, T., and C. Peskin. 2000. The role of protein flexibility in molecular motor function: Coupled diffusion in a tilted periodic potential. SIAM J. Appl. Math. 60:842-867.
40. Astumian, R. D. 2007. Adiabatic operation of a molecular machine. Proc. Natl. Acad. Sci. USA 104:19715-19718.
41. Chemla, Y. R., K. Aathavan, J. Michaelis, S. Grimes, P. J. Jardine, D. L. Anderson, and C. Bustamante. 2005. Mechanism of force generation of a viral DNA packaging motor. Cell 122:683-692.
42. Yasuda, R., H. Noji, K. Kinosita, and M. Yoshida. 1998. $F_1$-ATPase is a highly efficient molecular motor that rotates with discrete 120° steps. Cell 93:1117-1124.
43. Kolomeisky, A. B., and M. E. Fisher. 2007. Molecular Motors: A Theorist's Perspective. Annu. Rev. Phys. Chem. 58:675-695.
44. Samuel, A. D., and H. C. Berg. 1995. Fluctuation analysis of rotational speeds of the bacterial flagellar motor. Proc. Natl Acad. Sci. USA 92:3502-3506.
45. Samuel, A. D., and H. C. Berg. 1996. Torque-generating units of the bacterial flagellar motor step independently. Biophys. J. 71:918-923.
46. Wang, H., and G. Oster. 1998. Energy transduction in the F1 motor of ATP synthase. Nature 396:279-282.
47. Khan, S., M. Dapice, and T. S. Reese. 1988. Effects of mot gene expression on the structure of the flagellar motor. J. Mol. Biol. 202:575-584.
48. Dan, N., P. Pincus, and S. A. Safran. 1993. Membrane-induced interactions between inclusions. Langmuir 9:2768-2771.
49. Block, S. M., D. F. Blair, and H. C. Berg. 1989. Compliance of bacterial flagella measured with optical tweezers. Nature 338:514-518.
50. Lauger, P. 1990. Microscopic Models of the Bacterial Flagellar Motor. Comments Theoret. Biol. 2:99-123.

## Table 1

| Quantity | | Value | Comments |
|---|---|---|---|
| Potential periodicity, $\delta$ | | $2\pi/26$ | Refs. (7, 17) |
| Rotor drag coefficient, $\zeta_R$ | | $2\times10^{-3}$ pN•nm•s/rad$^2$ | Estimated |
| Bead diffusion constant, $D_L$ | | 0.01–100 rad$^2$/s | Calculated from Stokes' Law |
| Stator diffusion constant, $Ds$ | | 500 rad$^2$/s | Estimated |
| Load-Rotor Linkage spring constant, $\kappa$ | | 400-500 pN.nm/rad$^2$ | Estimated from experimental measurements (49) |
| Saw-tooth potential height, $U$ | | 10 $k_BT$ | Ad hoc |
| Ratio of the two potential branches, $L_{\text{left}}/L_{\text{right}}$ | | 1/9 | |
| Potential bumps | Height | 15 $k_BT$ | |
| | Width | $0.2\delta$ | |
| | Centers | $0.1\ \delta$ (State1)<br>$0.6\ \delta$ (State 2) | |
| Transition windows | $\alpha_{1.},\alpha_2$ | $0.1\ \delta$, $0.6\ \delta$ | Fitting data |
| | $\beta_1,\beta_2$ | $0.58\delta$, $(0.58+0.5)\ \delta$ | |
| Binding site pK value | $H^+$ motor | $pK_a= 7.3$ | Estimated (using the middle value of external and internal concentration) |
| | Chimera motor | $pK_a= 31.6$mM | |
| Binding rate pre- | $H^+$ motor | $1.0\times 10^{20}\ s^{-1}$ | Fit experimental torque-speed |

|  |  |  |  |
|---|---|---|---|
| factors (two ions) $k_0$ | Chimera motor | $1.0\times 10^{8}$ $s^{-1}$ (or $6.0\times 10^{7}$ $s^{-1}$ with a uniform window) | curve |
| *E.coli* BFM living condition | $pH_{periplasm}$ | 7.0 | Experimental values |
|  | $pH_{cytoplasm}$ | 7.6 |  |
|  | $V_{membrane}$ | 120mV |  |
| Chimera BFM living condition | $[Na]_{periplasm}$ | 85mM |  |
|  | $[Na]_{cytoplasm}$ | 12mM |  |
|  | $V_{membrane}$ | 140mV |  |

**Table 1 Model parameters.**

# Figure Captions

Figure 1 Schematic illustration of (a) the flagellar motor structure and (b) the mathematical model. There are three essential components in the model to reproduce the observed motor torque-speed relations: a) a potential barrier to reduce futile backward slipping after a power stroke and ensure tight coupling; b) an elastic linkage between the motor and the bead; c) localized chemical transitions. (reproduced from ref. (25) with permission) (c) definition of the angular variables $\theta_S, \theta_R, \theta_L$ used in our simulations.

Figure 2 The experimental (triangles) and calculated (solid lines) torque-speed curves for (a) the *E. coli* $H^+$ and (b) the chimera BFM motors. Normalized torque is used in both figures. In (b) we show two model predictions: solid line, the same transition assisting window as used in *E. coli* fitting; dashed line, a uniform transition window.

Figure 3 Different effects of the two energy components on *E. coli* motor dynamics: (a) with fixed ion concentrations but varying membrane potential; upper inset panel: motor speed vs. membrane voltage along a high load (D = 0.15 $\mathbf{rad^2/s}$) line; lower inset panel: motor speed vs. membrane voltage along a low load (D = 2.1$\mathbf{rad^2/s}$) line. (b) with fixed membrane potential but varying external ion concentration; upper inset panel: motor speed vs. periplasm pH along a high load (D = 0.15 $\mathbf{rad^2/s}$) line; lower inset panel: motor speed vs. periplasm pH along a low load (D = 2.1 $\mathbf{rad^2/s}$) line. (c) with fixed ion motive force but different portion of membrane potential and ion concentration difference; inset panel: comparison of motor speed at high load and low load with fixed IMF. Here we show results for the $H^+$ motor. Similar results are obtained for the chimera motor.

Figure 4 The zero-load speed of an 8-stator *E. coli* motor compared to the zero-load speed of 1-stator motor with different stator spring constant (different lines are obtained with different stator diffusion constant)

Figure 5 Single molecule trajectories of the chimera motor at different external $Na^+$ concentrations. (a) Simulations. (b) Experimental data from ref (17). (c) Schematic illustration of the stepping behavior. The labels in (a) and (c) are consistent. 1: local fluctuation within a potential well. 2: fast transient sliding along a potential after chemical transition. 3: backward slipping which breaks tight coupling. 4: backward motion with tight coupling between motor motion and chemical transitions. To make easy

connection between the continuous model and other discrete kinetic models (e.g., (50)), we indicated the corresponding motor mechanchemical states ‘PE’, ‘PO’, ‘CE’, ‘CO’, where ‘P’ and ‘C’ refer to that the ion binding sites are accessible from the periplasm and cytoplasm sides, respectively, ‘E’ and ‘O’ mean that the binding sites are empty and occupied, respectively.

Figure 6 Predicted *E. coli* BFM stepping behavior for one stator with stator spring constant $\kappa = 200$ pN nm/rad$^2$ (left column) and $\kappa = 3000$ pN nm/rad$^2$ (right column) by analyzing 10 s long trajectories. Same parameters as in Table 1 except for $pH_{periplasm}=8.4$ (a) a typical trajectory (the solid lines are steps found by the step finding algorithm) ; (b) the stepping size distribution; (c) the stepping dwelling time distribution.

Figure 7 Stepping behaviors with two stators. (a) With stiff stator springs, the motor may generate substeps reflecting the distance between the two stators $\Delta\theta_S$ relative to the rotor periodicity $\delta$. If the ratio $\Delta\theta_S / \delta$ is not integer, smaller substeps may be observed. (b) If the ratio $\Delta\theta_S / \delta$ is integer, the stepsize is the same as in the case of one stator, but the dwelling time is longer on average. (c) With soft stator springs, chemical transition within one stator is not restricted by the other stator.

Figure 8 Predicted *E. coli* BFM stepsize distributions with two stators by analyzing 2 s long trajectories with a step-finding algorithm. (a) two stators offset by 0.5 $\delta$, stator spring $\kappa = 3000$ pN nm/rad$^2$; (b) two stators offset by $\delta$, stator spring $\kappa = 3000$ pN nm/rad$^2$; (c) two stators offset by 0.5 $\delta$, stator spring $\kappa = 200$ pN nm/rad$^2$; (d) two stators offset by $\delta$, stator spring $\kappa = 200$ pN nm/rad$^2$;

# Figures

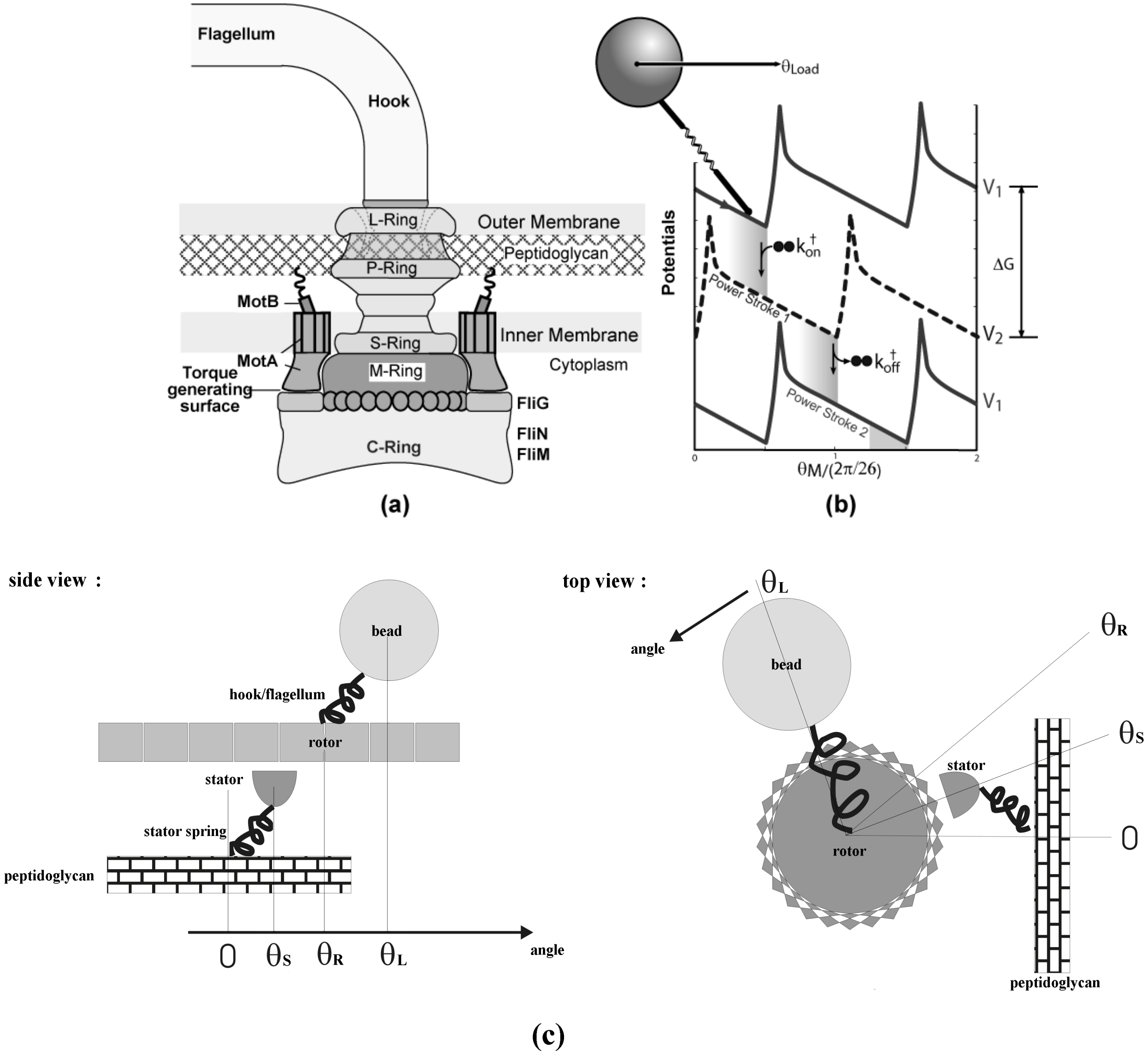
Flagellum
Hook
L-Ring
Outer Membrane
Peptidoglycan
P-Ring
MotB
Inner Membrane
S-Ring
MotA
Torque generating surface
M-Ring
Cytoplasm
FliG
FliN
FliM
C-Ring
(a)
$\theta_{Load}$
Potentials
$V_1$
$\Delta G$
$k_{on}^{\dagger}$
Power Stroke 1
$V_2$
$k_{off}^{\dagger}$
$V_1$
Power Stroke 2
0
1
2
$\theta M/(2\pi/26)$
(b)
side view :
bead
hook/flagellum
rotor
stator
stator spring
peptidoglycan
0
$\theta_S$
$\theta_R$
$\theta_L$
angle
top view :
$\theta_L$
angle
bead
$\theta_R$
$\theta_S$
stator
0
rotor
peptidoglycan
(c)

Figure 1 Bai et al.

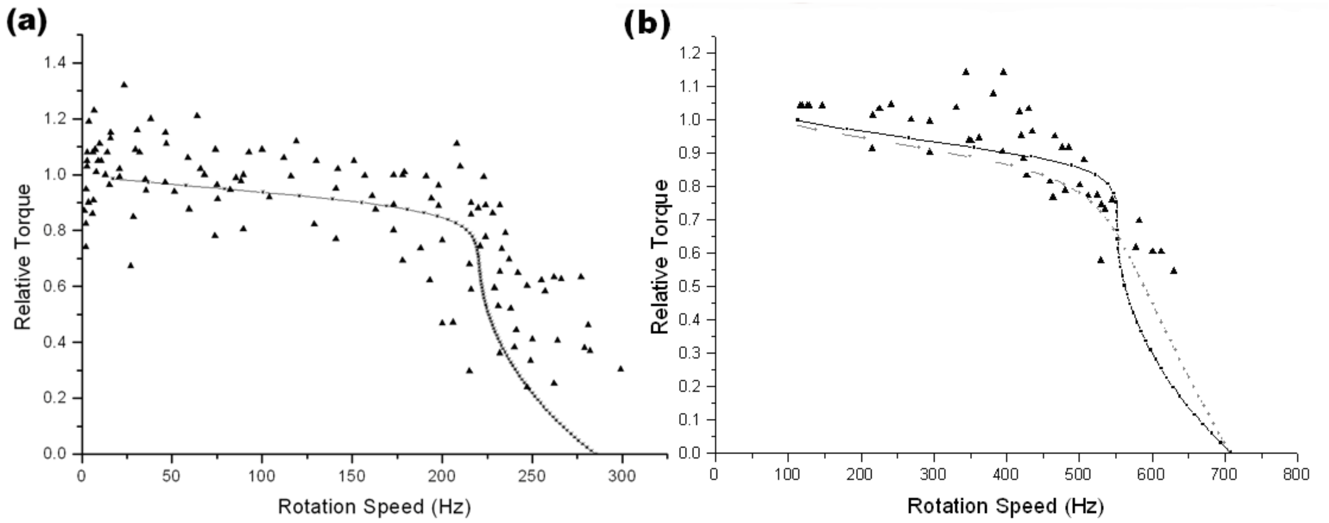

Figure 2 Bai et al.

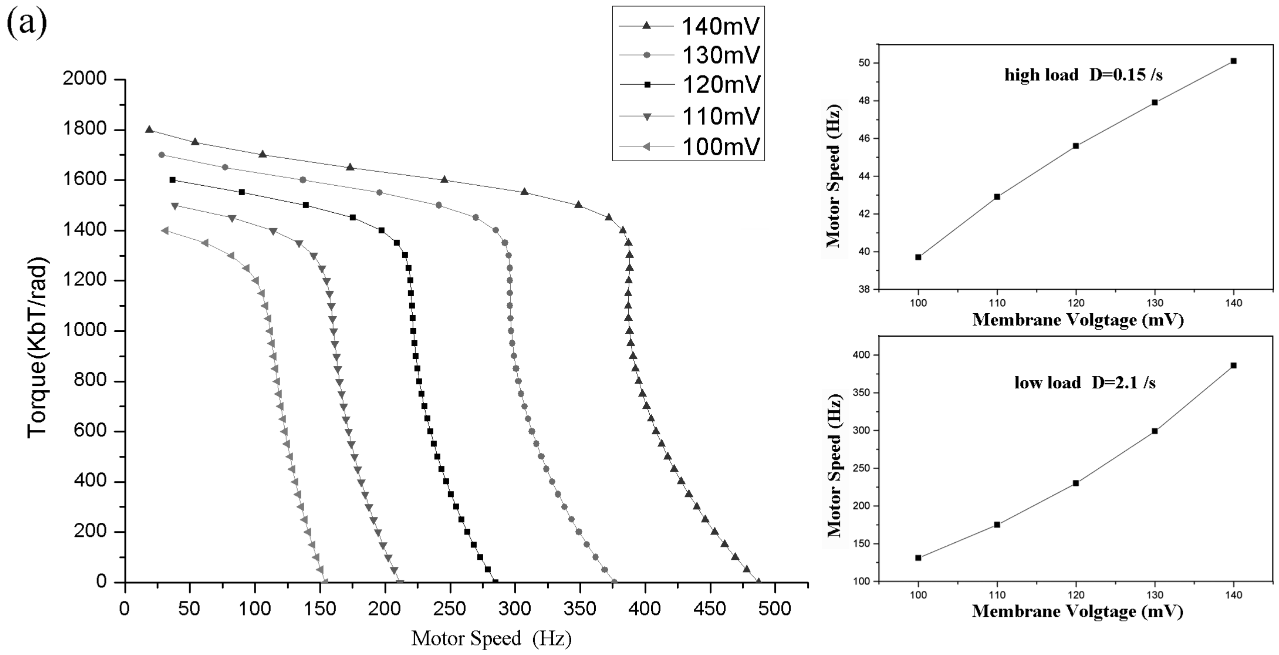

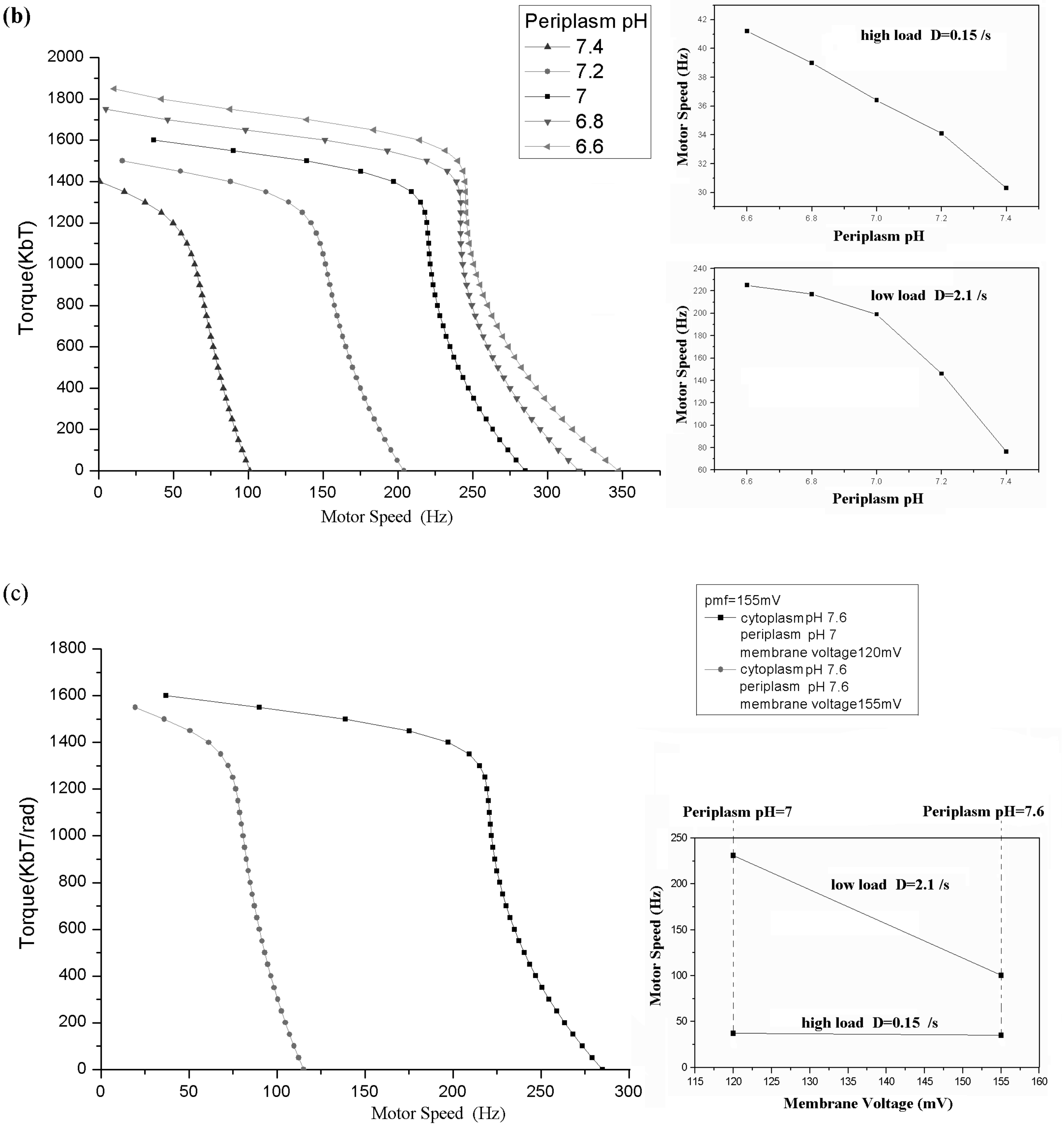

Figure 3 Bai et al.

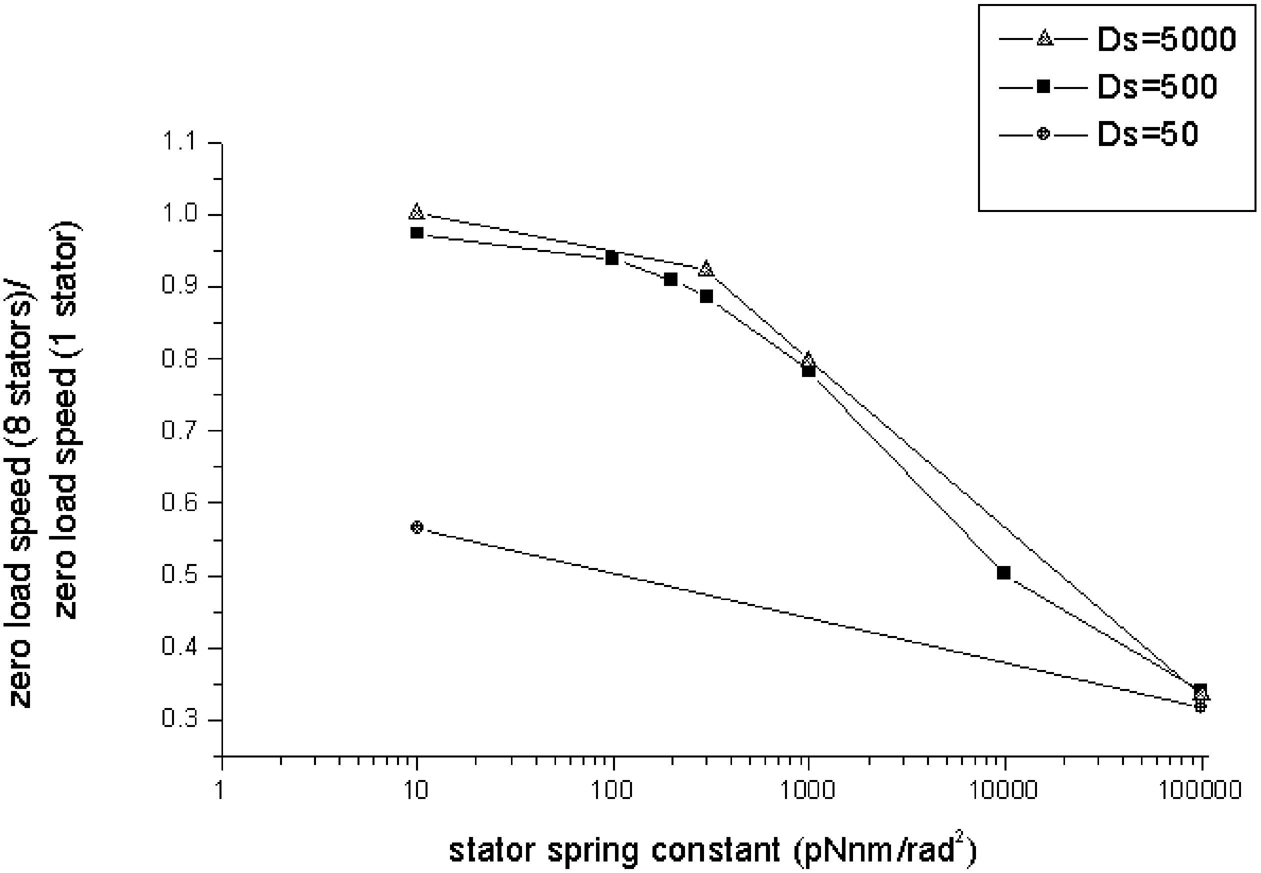

Figure 4 Bai et al.

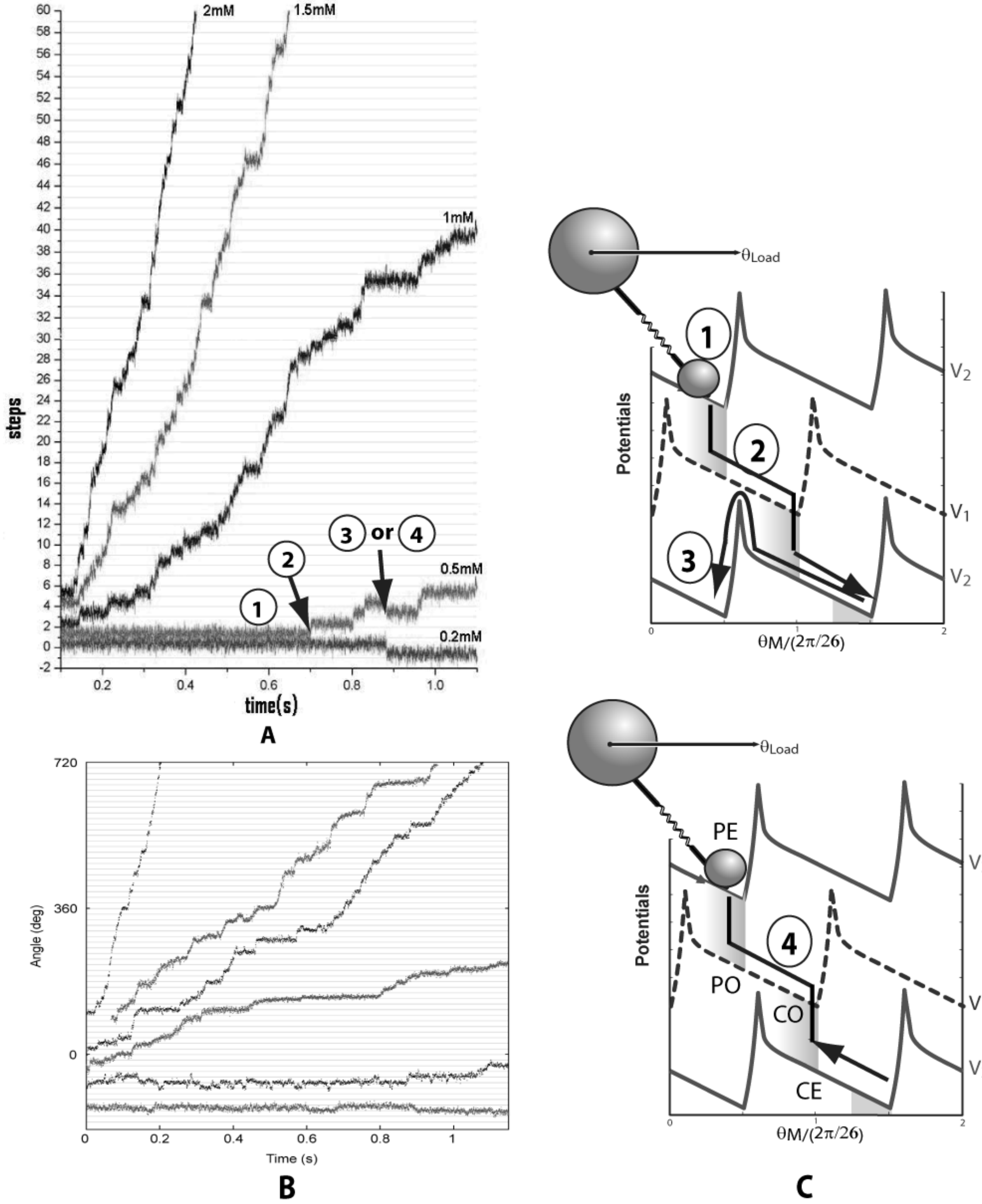

Figure 5 Bai et al.

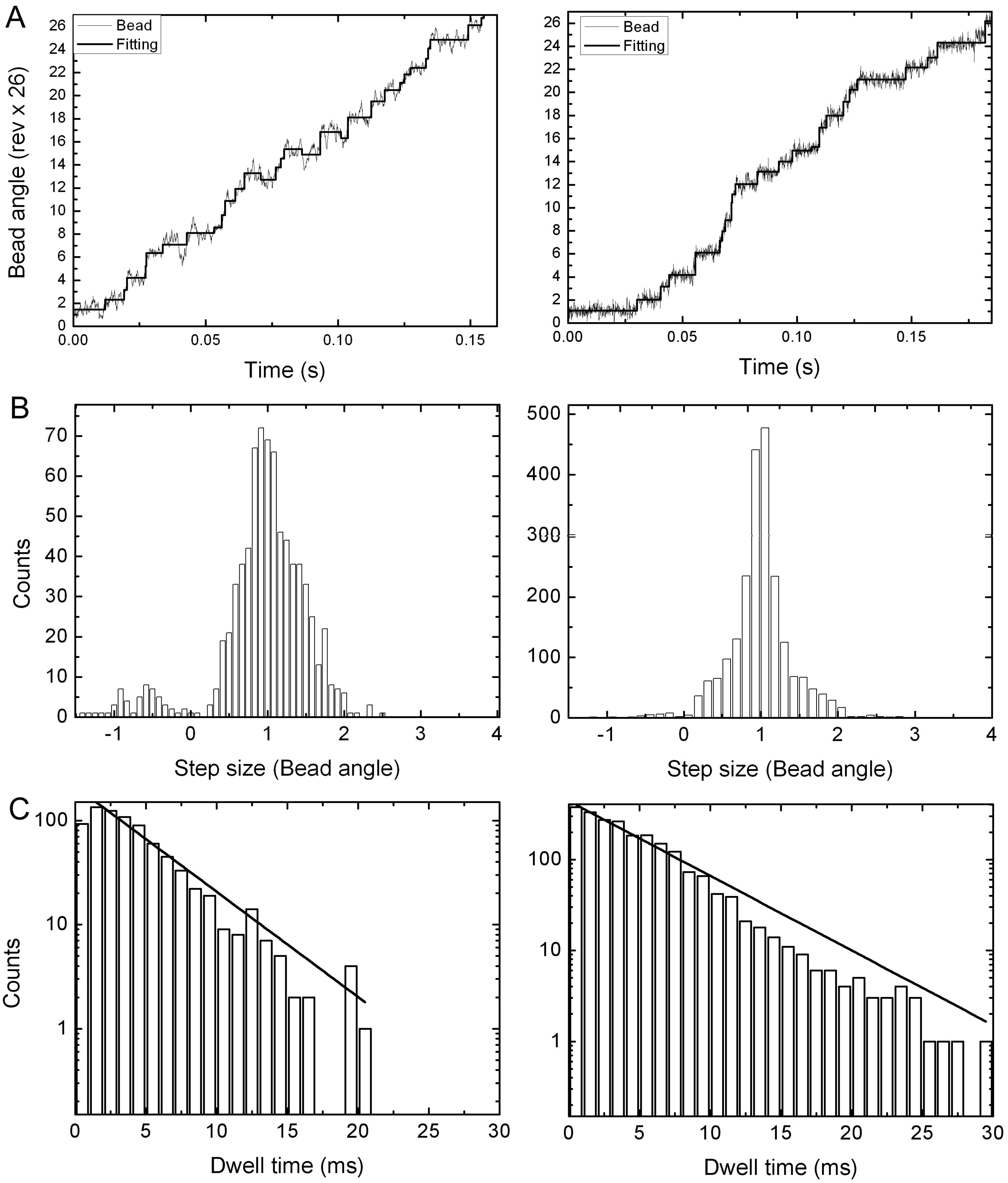

Figure 6 Bai et al.

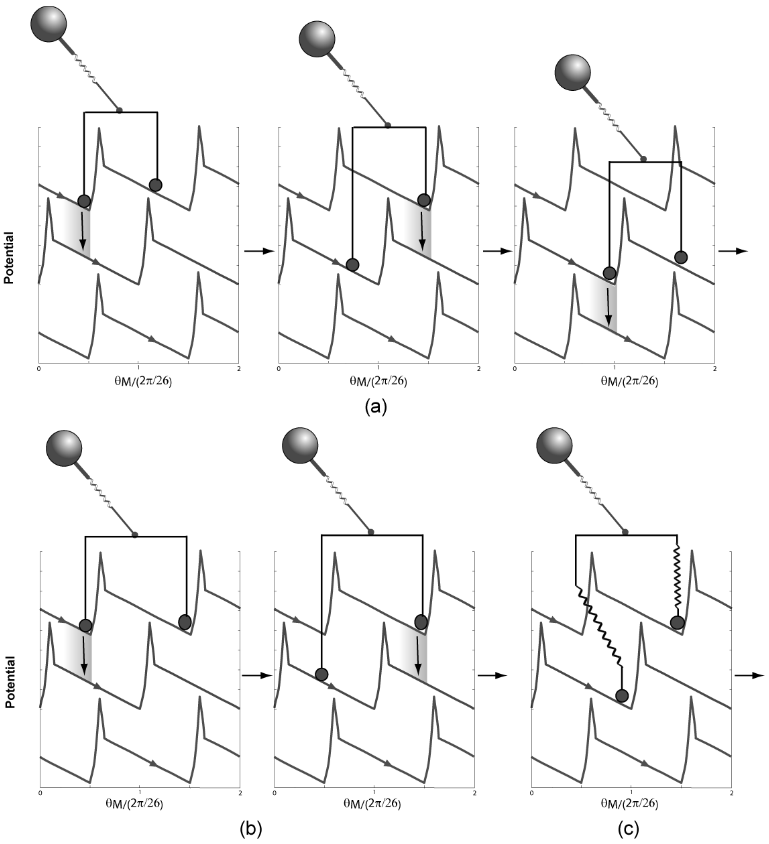
Potential
θM/(2π/26)
0
1
2
(a)
(b)
(c)

Figure 7 Bai et al.

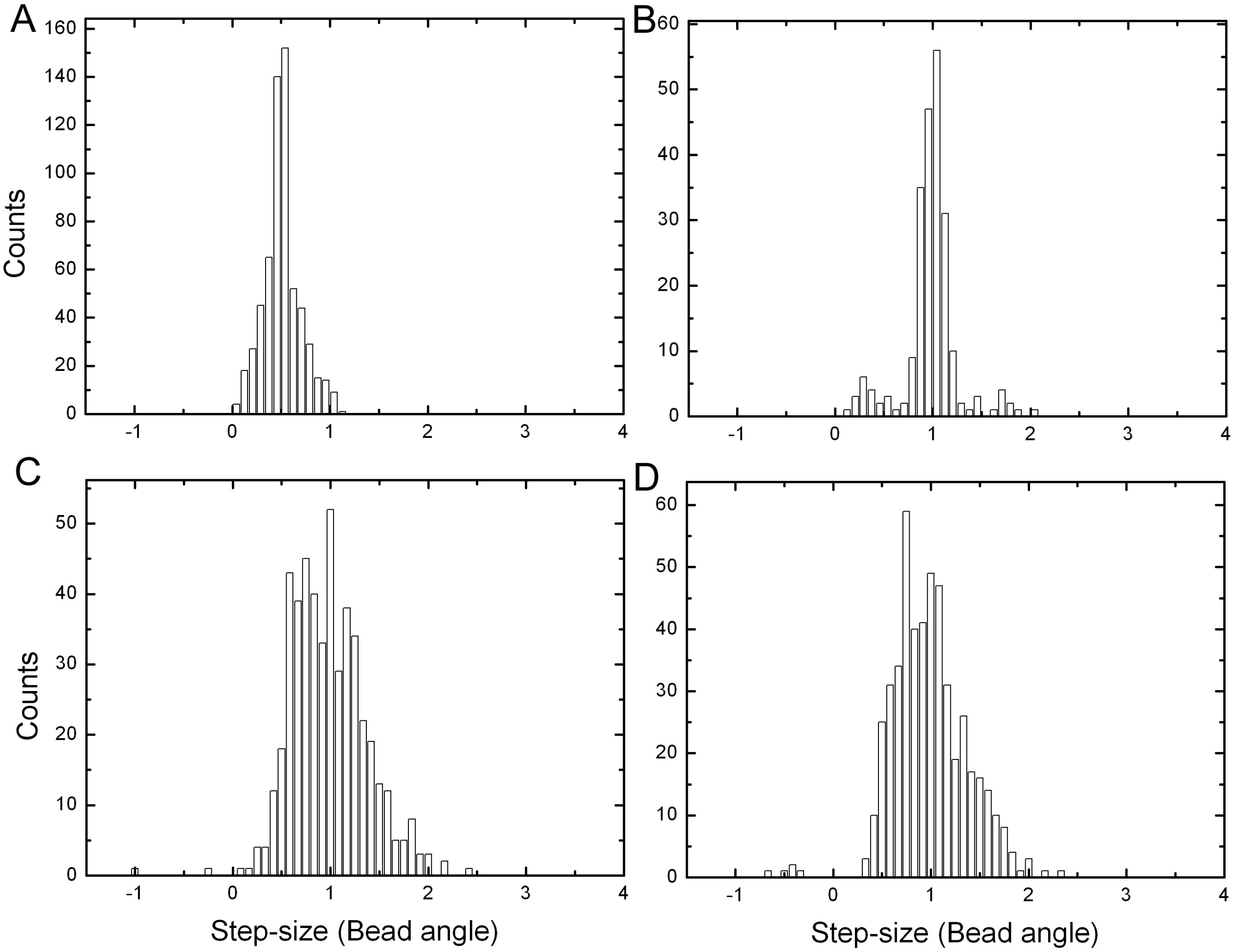

Figure 8 Bai et al.